AIAA JOURNAL
Vol. 30, No. 2, February 1992

Laser Velocimetry Seed Particles Within Compressible, Vortical Flows

Mark S. Maurice*
Wright Laboratory, Wright-Patterson Air Force Base, Ohio 45433

The ability of seed particles to penetrate and accurately track vortices is of critical importance to the analysis of laser velocimetry (LV) measurements within these flow structures. In applying a particle equation of motion to vortical flowfields which extend into the supersonic, compressible regime, two approaches are considered. First, an ideal, potential vortex is developed for a compressible flowfield. As an aid to the design and analysis of vortical flowfield surveys over a wide range of independent parameters, this model is used to plot the time and position at which any particle starting at rest within a vortex will begin to track the flow velocity within 3% error. As a specific application, the potential vortex is then used to estimate the dynamic bias of LV measurements taken within a vortex shed from a 75-deg delta wing at 20 deg angle of attack in a Mach 1.9 supersonic flow. The second approach uses a computationally derived Navier-Stokes flowfield solution in place of the potential vortex model. The computational flowfield method predicts that accurate LV measurements within the delta wing flowfield require seed particles no larger than 0.1–0.2 μm in diameter, and defines the unseeded inner vortex core region. Both approaches show an increase in velocity bias which is nearly proportional to particle diameter, stressing the need for a monodisperse seed of known size to resolve particle bias in complex flows.

Nomenclature

Cd = drag coefficient, Eq. (15)
Cd_1 = function defined by Eq. (16)
Cp = specific heat
d = particle diameter
G = function defined by Eq. (17)
h = function defined by Eq. (18)
L = root chord length
M = Mach number
m = mass
P = pressure
R = gas constant
Re_0 = Reynolds number, Eq. (2)
r = radial spacial coordinate
$\hat{r}$ = transformed, dimensionless radial coordinate, Eq. (12)
S = Sutherland viscosity constant
St = Stokes number, Eq. (4)
s = distance, used in Eq. (6)
T = temperature
t = time
u = fluid velocity
v = particle velocity
w = modified particle relative velocity, Eq. (14)
x,y,z = Cartesian spacial coordinates
$\%ERR$ = measure of particle velocity bias, Eqs. (24) and (25)
α = angle of attack
β = density ratio, Eq. (3)
Γ = circulation
γ = ratio of specific heats
θ = angular spacial coordinate in a cylindrical system
μ = molecular viscosity
π = dimensionless variable groups, Eqs. (26–28)
ρ = density
τ = dimensionless time, Eq. (23)
ω = vorticity

Subscripts
f = fluid property
i,j = Cartesian coordinate indicial notation
o = property in the outer field of a two-dimensional vortex
p = particle property
R = the relative difference between the particle and the fluid
0 = initial condition

Received Sept. 14, 1990; presented as Paper 91-0292 at the AIAA 29th Aerospace Sciences Meeting, Reno, NV, Jan. 7–10, 1991; revision received April 2, 1991; accepted for publication April 24, 1991.

*Mechanical Engineer, WL/FIMN. Member AIAA.

Introduction

THE dynamics of small particles within aerodynamic flowfields are of interest for a variety of applications. In propulsive engines, for example, combustion particles can have an erosive effect on turbine blades, as well as contributing to performance losses through the exit nozzle. External aerodynamic and control surface degradation can be strong functions of atmospheric dispersion, and sediment transport can be modeled by the dynamics of individual particles. In the application of flow visualization or laser velocimetry, however, it is required that the particle dynamics of the seed material describe the fluid dynamics of the flowfield. The seed particles are assumed to follow the fluid streamlines, and not to alter the corresponding unseeded flow.

In flow regions with large gradients such as near shock waves, or regions with high turbulence frequencies, particle dynamic bias can dominate laser velocimetry (LV) measurements. For the case of a seed particle passing through a shock wave, it has been shown by Nichols[1] that the particle lag can be substantial. If the mean velocity and turbulence intensity are determined from ensembled averages from a variety of particle sizes passing through the shock wave and measured at a single downstream location, these quantities may be grossly overestimated. On the other hand, it has been shown by Hjelmfelt and Mockros[2] that a particle subjected to a high-frequency, oscillating flowfield may greatly underestimate the turbulence intensity of the fluid.

Although fluid streamlines are circular within a two-dimensional potential vortex, centrifugal forces can cause seed particles to move radially away from the vortex origin. Consequently, LV velocity measurements within vortical flowfields[3-5] may be biased. For an incompressible, potential vortex flow, velocity bias can be computationally investigated using a simplified equation of motion derived by Dring and Suo,[6] who prescribe particle position in terms of three dimensionless parameters that are constant throughout the flow. For this case,

$$\frac{r}{r_0} = f(Re_0, \beta, St) \tag{1}$$

where

$$Re_0 = \frac{\rho_f v_0 r_0}{\mu} \tag{2}$$

$$\beta = \rho_f / \rho_p \tag{3}$$

and

$$St = \frac{\rho_p v_0 d^2}{18 r_0 \mu} \tag{4}$$

For compressible flow, all three independent parameters vary radially through the vortex. If these variables are held constant by defining them in terms of the total density and temperature of the flowfield, and trajectories are computed by an equation of motion which includes compressibility effects, it can be seen in Fig. 1 that as the initial Mach number of the particle increases into the compressible flow regime, the particle trajectory shows a substantial increase in bias. Consequently, in a compressible, vortical flow, an incompressible analysis can underestimate the particle velocity bias.

Approach

Potential Vortex

Although classical text book derivations assume the potential vortex to be an incompressible flow when deriving the velocity field,[7,8] the approach is extendible to compressible flowfields. In a compressible or incompressible flow, the potential vortex field is irrotational. Therefore, it is required that

$$\omega_x = \frac{\partial u_\theta}{\partial r} + \frac{1}{r}\left(u_\theta - \frac{\partial u_r}{\partial \theta}\right) = 0 \tag{5}$$

Since a potential vortex has no radial velocity component, and since the angular velocity component is only a function of radial distance, Eq. (5) reduces to a first-order ordinary differential equation with an integration constant related to the vortex strength by the application of Stokes' theorem:

$$\Gamma = -\oint \boldsymbol{u} \cdot d\boldsymbol{s} \tag{6}$$

The resulting vortex velocities are

$$u_\theta = \frac{-\Gamma}{2\pi r} \tag{7}$$

and

$$u_r = 0 \tag{8}$$

Since this velocity field satisfies the compressible form of the continuity equation, the flowfield is physically possible. If the radial direction of the vortex lies on the y-z plane of a Cartesian coordinate system, the two-dimensional vortical field can be superimposed with a constant normal velocity in the x direction. The resulting three-dimensional flowfield will then have helical streamlines that rotate about the x axis. This flowfield can be used as a simple model of vortices that are shed from aerodynamic surfaces, recognizing that it does not account for axial variations of vortex strength or the development of a viscous core.

Another consideration for a potential vortex in a compressible flow is the limit of the mathematical model. For the incompressible case, the temperature is considered constant throughout the field, leaving only the infinite velocity at the center of the vortex as a limit. In a compressible flow, however, the temperature decreases toward zero as the velocity becomes infinite. To examine the inner limit with respect to commonly used constitutive equations for thermodynamic closure, it is best to temporarily decouple the constant axial velocity from the vortical flow plane. Since the flow can be considered isentropic and adiabatic, the axial velocity can be used to relate the total temperature, pressure, and density of the flowfield to the static values in the outer vortex region which approaches zero velocity in the vortical flow plane. These "outer" values can then be considered as stagnation values for the decoupled two-dimensional vortex flowfield. Within the region of the flowfield where the perfect gas law and calorically perfect gas assumption hold,

$$\frac{T}{T_o} = (\hat{r}) \tag{9}$$

$$\frac{P}{P_o} = (\hat{r})^{\gamma/(\gamma-1)} \tag{10}$$

and

$$\frac{\rho}{\rho_o} = (\hat{r})^{1/(\gamma-1)} \tag{11}$$

where

$$\hat{r} = 1 - \frac{\Gamma^2}{8\pi^2 r^2 C_p T_o} \tag{12}$$

The thermodynamic profiles in terms of the transformed radial coordinate are shown in Fig. 2. For air, the stagnation temperature within the vortical plane can be as high as 470 K, based on an arbitrary maximum of 2% error in the calorically perfect gas assumption. The inner limit of the model, based on a maximum 3% error in Sutherland's viscosity law, is at radial distance from the vortex origin where the stagnation temperature has decreased to 167 K.

The corresponding range of P_o extends from near vacuum to an upper limit defined by the validity of the perfect gas law. For a maximum 2% error, any P_o up to 11.2 atm is valid over the entire range of T_o.

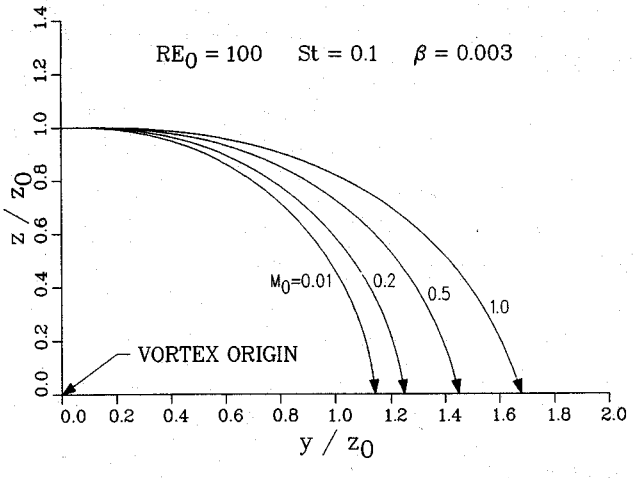

Fig. 1 Particle trajectories within a potential vortex in a compressible flow.

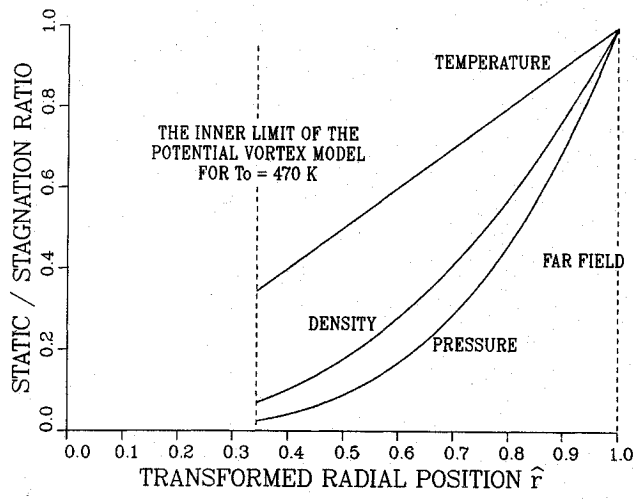

Fig. 2 Thermodynamic profiles through a potential vortex in a compressible flow.

Particle Equation of Motion

The equation set used to describe the particle motion is developed by Nichols,[9] and includes the influences of Stokes' drag, resultant pressure, apparent mass, gravitational forces, and the Basset history integral. For application to the vortical flow, the gravitational term and the Basset history integral have been excluded. The Basset term can be significant when the particle density is of the same order of magnitude as the fluid density, or when the particle relative acceleration is large compared with the particle relative velocity. In this case, as in most numerical solutions, the Basset term is neglected because the numerically evaluated integral is found to be either negligible, highly unstable, or potentially biased by the accumulation of roundoff and truncation errors. The resulting differential equation for a general steady-state flow can be written as

$$\frac{dv_i}{dt} = \frac{-3C_d}{4d}\frac{m_f}{(m_p + m_f/2)} w_i|w| + \frac{m_f}{(m_p + m_f/2)} u_j \frac{\partial u_i}{\partial x_j} + \frac{m_f}{(m_p + m_f/2)} \frac{d}{dt}\left\{u_i + \frac{d^2}{40}\nabla^2 u_i\right\} \tag{13}$$

where

$$w_i = v_i - u_i - \frac{d^2}{24}\nabla^2 u_i \tag{14}$$

and each of the fluid properties and derivatives are evaluated with respect to the particle location.

The drag coefficient is evaluated by the drag law of Crowe[9,10]:

$$Cd = (Cd_1 - 2)\exp\{-3.07\gamma^{1/2}(M_R/Re_R)G(Re_R)\} + \{h(M_R)/(\gamma^{1/2}M_R)\}\exp\{-Re_R/(2M_R)\} + 2 \tag{15}$$

where

$$Cd_1 = \frac{24}{Re_R}(1 + 0.158Re_R^{2/3}) \tag{16}$$

$$\log_{10}G(Re_R) = 1.25\{1 + \tanh(0.77\log_{10}Re_R - 1.92)\} \tag{17}$$

and

$$h(M_R) = \{2.3 + 1.7(T_p/T_f)^{1/2}\} - 2.3\tanh(1.17\log_{10}M_R) \tag{18}$$

Crowe's drag law is valid over a wide range of relative Reynolds and Mach numbers, and includes the effects of inertia, compressibility, rarefaction, and heat transfer.

Nichols[9] shows that the particle equation of motion becomes stiff for small particle diameters. Consequently, his solutions for particle behavior through shock waves are piecewise, using Adams' technique where possible, and restarting the solution with slower Runge-Kutta integration when local stiffness causes Adams' method to diverge. To avoid the necessity of piecewise solutions while maintaining computational efficiency, solutions presented here are obtained by 4th order Runge-Kutta-Fehlberg (RKF) numerical integration. The RKF method is ideally suited for this situation since it estimates the local stiffness of the equation at each time step, and adjusts the step size accordingly. Results include a general consideration of trajectories and velocity bias within the potential vortex model, specific application of the model to an experimental LV survey, and the use of a computational fluid dynamics (CFD)-generated vortical flowfield in place of the model.

Results

Dimensional Analysis

The particle equation of motion described by Eq. (13) requires the coupled solution of three first-order differential equations initialized by particle position and velocity within a specified vortical field. To reduce the equation set for analysis, consider the slightly more specific case of an LV seed particle traveling downstream in airflow (in the x direction), and at time zero, it becomes surrounded by a potential vortex. If the particle is traveling with the same initial constant downstream velocity as the flow, the equation of motion for the x direction decouples from the vortical flow in the y-z plane. Since there are no initial forces on the particle in the x direction, the equations show that the downstream particle velocity will remain constant. Additionally, since the vortex is axisymmetric, one initial condition parameter can be eliminated by choosing y_0 as the initial particle position, and setting z_0 to zero. Also, since the particle is assumed to have no initial velocity other than in the x direction, both of the initial velocity parameters in the vortical plane can be set to zero.

Analysis of the reduced equation set in the vortical plane coupled with the various equations of closure require the following dimensional inputs:

$$u_0, \rho_o, T_o, \mu_o, S, d, \rho_p, y_0 \tag{19}$$

where S is Sutherland's constant for air, and the outer viscosity can be evaluated by Sutherland's law for the input value of T_o. These dimensional inputs describe the dependent variables:

$$y, z, v_y, v_z, t \tag{20}$$

Application of the Buckingham Π Theorem[7,8] reduces the dimensional equation set to a function in terms of five dimensionless, independent parameters:

$$\frac{T_o}{S}, \frac{u_0^2}{RT_o}, \frac{\rho_o u_0 d}{\mu_o}, \frac{\rho_p}{\rho_o}, \frac{y_0}{d} \tag{21}$$

Additional trial-and-error analysis shows that the effect of the parameter involving Sutherland's constant is negligible, and that the density ratio and initial distance parameters can be combined. The resulting dimensionless equation set is

$$\frac{y}{y_0}, \frac{z}{y_0}, \frac{v_y}{u_0}, \frac{v_z}{u_0}, \tau = f\left\{\frac{u_0^2}{RT_o}, \frac{\rho_o u_0 d}{\mu_o}, \frac{y_0\rho_o}{d\rho_p}\right\} \tag{22}$$

where

$$\tau = tu_0/y_0 \tag{23}$$

Two of the dependent dimensionless parameters in Eq. (22) describe the particle velocities in the vortical plane. However,

describe the particle velocities in the vortical plane. However, for application to LV, it is the bias in these quantities that is important. Therefore, define

$$\%ERR_y = \frac{v_y - u_y}{(u_y^2 + u_z^2)^{1/2}} \times 100 \quad (24)$$

$$\%ERR_z = \frac{v_z - u_z}{(u_y^2 + u_z^2)^{1/2}} \times 100 \quad (25)$$

Since these two error parameters can be written as functions of the dimensionless groups, they can be used as dependent dimensionless parameters themselves.

The three independent dimensionless groups can be fully defined by inputs of outer temperature and density, initial flowfield velocity and particle position, and the particle density and diameter. In terms of dimensionless variables, these groups can be defined as

$$\pi_1 = u_0/(RT_o)^{1/2} \quad (26)$$

$$\pi_2 = \rho_o u_0 d/\mu_o \quad (27)$$

$$\pi_3 = (y_0\rho_o)/(d\rho_p) \quad (28)$$

The six independent dimensional parameters and the viscosity from Sutherland's law are bounded for LV purposes in Table 1. The corresponding ranges of the three π parameters are also shown.

Particle trajectories in the y-z plane for a single combination of π groups are shown in Fig. 3. For this case, the particle has moved to more than twice its initial radial position after three helical revolutions. Although the trajectory alone does not quantify the velocity bias, it does show the difficulty in maintaining seeded flow near the vortex origin.

For the same combination of π groups, the measurement error that will occur in the y and z velocity components as a function of dimensionless time is shown in Fig. 4. In general, the magnitude of velocity bias decreases from 100% at the initial condition toward 0% as the particle moves outward from the vortex origin to a radius where it accurately follows the fluid streamlines. Since the velocity normal to the vortical plane is constant, values of τ correspond linearly to particle translation along the x axis.

For the ranges of parameters selected in Table 1, the radial particle position and corresponding time at which the total magnitude of velocity bias decreases to 3% is shown in Figs. 5a–5c. On the log-log scale, the curves of radial position are shown to decrease nearly linearly towards conditions where any radial displacement of the particle is negligible. In terms of the dimensional parameters, this decrease corresponds to smaller particle diameters, an initial position further from the vortex origin, or lighter particles relative to the fluid density.

The corresponding curves for τ also decrease as π_3 increases, and include a sharp drop at the point where radial translation becomes negligible. In general, damping the velocity bias from the initial conditions is much faster than any required radial translation of the particle. Consequently, the portion of the curve above the dip is for particles that must be translated further away from the vortex origin, while the portion of the curve below the dip corresponds to particles that are brought from rest to the fluid velocity at the initial radial particle position.

Application of the Potential Vortex

As a specific application, the potential vortex is used to model an LV measured supersonic vortex shed from a 75-deg delta wing at 20-deg angle of attack. The two-dimensional velocity vector field at 80% chord is shown in Fig. 6, and a comprehensive description of the experimental test and results can be found in Ref. 5. From the known stagnation conditions and freestream Mach number, the outer vortex temperature, density, and axial velocity are determined, and the density of the seed corresponds to the 10 cS silicon oil that was used for the test.

Three-dimensional LV measurements were made in the plane perpendicular to the model surface. However, it was found that by applying a rotational transformation to the data, lines emanating normal from the individual two-dimensional velocity vectors tend to converge towards a point. This point is estimated to be the vortex origin. The transformed velocity field shown in Fig. 6 corresponds to a "vortex angle of attack" of 8 deg from the freestream flow.

The corresponding values of vortex strength decrease from the outer edge of the wing towards the delta wing centerline. For this example, a nominal weighted average value of -50 m^2/s is used.

Using the inner limit of the potential vortex model as an initial position, the corresponding particle trajectories for various sizes of seed are shown in Fig. 7. Because of the high speed of the axial flow, the particles only travel about one-third of a helical revolution from the nose of the wing to the 80% chord location. However, the difference in individual trajectories is significant, showing a nearly circular path for the 0.1-μm particle while the 5.0-μm particle increases its radial distance from the vortex origin by more than 40%.

The radial position of particles at the 80% chord location as a continuous function of seed diameter is given in Fig. 8. Over the included range of 0.1–5.0 μm particles, the curve shows that the increase in radial translation is fairly linear.

The corresponding curve of the velocity bias at this chord location is given in Fig. 9. This curve is also fairly linear, showing a steady increase in bias from less than 0.5% for 0.1-μm particles to nearly 28% for 5.0-μm seed. This curve shows that seed diameters of the polydispersed silicon oil must be less than 0.833 μm in order to maintain a velocity bias of less than 3.0%.

Finally, the measurement error for three candidate particle sizes as a function of chord position is shown in Fig. 10. In each case, the particle bias at zero percent chord is 100%,

Table 1 Chosen ranges of dimensional and corresponding dimensionless parameters

Parameter	Range	Reasoning
T_o, K	176–470	The lower value is arbitrarily chosen so that $M \geq 0.5$ at the inner limit of the vortex model. The upper value is based on a maximum 2% error for the calorically perfect gas assumption.
ρ_o, kg/m^3	0.0375–4.011	Dependent on T_o, this range corresponds to the minimal range of 0.05 atm $< Po <$ 2 atm, which is an arbitrary range of interest.
μ_o, kg/ms	1.19E−5–2.56E−5	From Sutherland's viscosity law for the range of To.
U_0, m/s	10–780	The lower value is arbitrary, the high value, dependent on To, is the velocity at the inner limit of the vortex model.
ρ_p, kg/m^3	260–3960	This range covers a wide variety of LV seed, from hollow glass spheres to Al_2O_3.
d, μm	0.2–100	This is a typical range for LV seed diameters.
y_0, m	0.001–2.0	This is a probable range of interest for wind-tunnel applications.
π_1	0.0273–2.144	π_1, π_2, and π_3 are based on appropriate combinations of dimensional parameters.
π_2	0.00293–12221	
π_3	9.47×10^{-5}–154269	

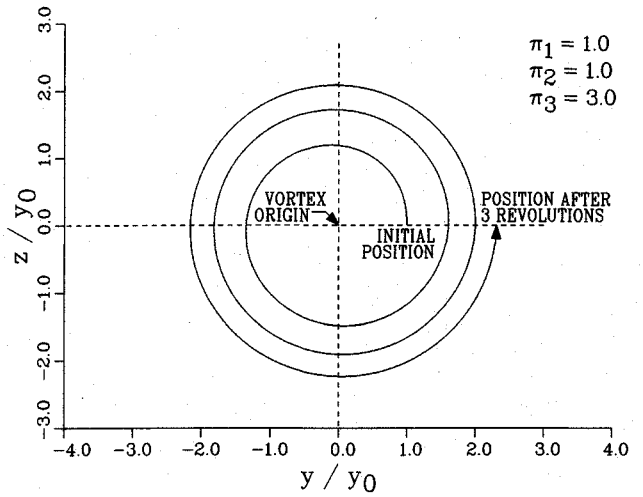

Fig. 3 Representative particle trajectory for one possible π group.

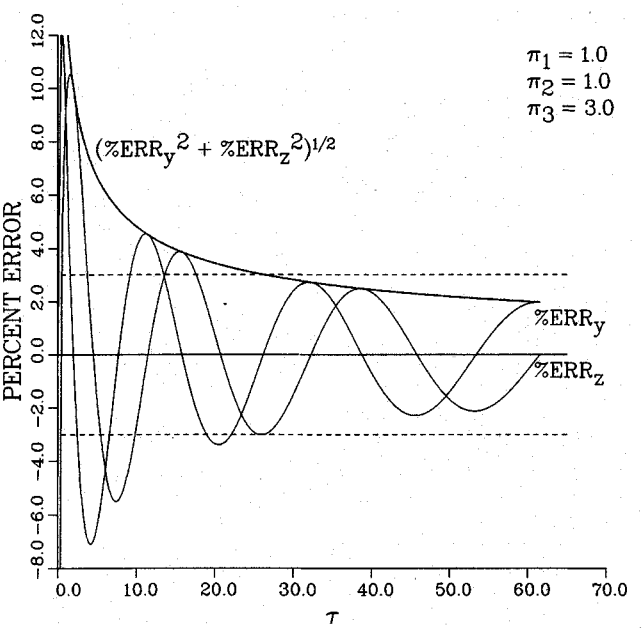

Fig. 4 Representative time history of velocity bias for one possible π group.

since the particles have no initial velocity in the vortical plane. By the time the particles move downstream only 2–5% chord, however, the initial bias is completely damped. The remaining bias is due to the tangential momentum of the particle in the vortical field, and slowly decays as the radial distance of the seed from the vortex origin increases.

Consequently, this example predicts that for seed particles of less than 0.833 μm in diameter, reasonably unbiased LV measurements can be made within the radial limits of the potential vortex model at any axial station downstream of about 10% chord. Since the inner bound of the model happens to be the approximate bound at which LV measurements were actually taken, the unmodeled viscous inner core of the vortex is inconsequential to this analysis. Furthermore, it was found that any possible initial velocities applied to the seed particles were quickly damped, making the results nearly independent of the simplified set of initial conditions used.

Application of a Computational Fluid Dynamics-Generated Vortical Field

As a second application of the particle equations of motion, the potential vortex model is replaced with a three-dimensional Navier-Stokes solution of a delta wing flowfield. For the same

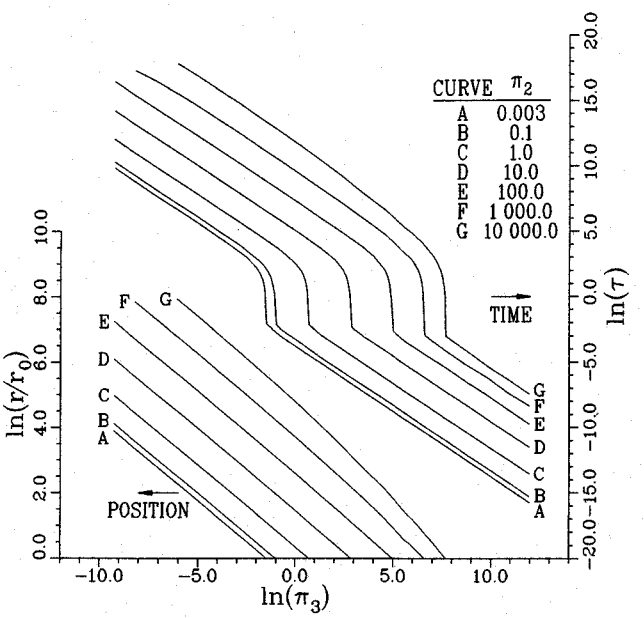

Fig. 5a Particle time and position at 3% velocity bias ($\pi_1 = 0.03$).

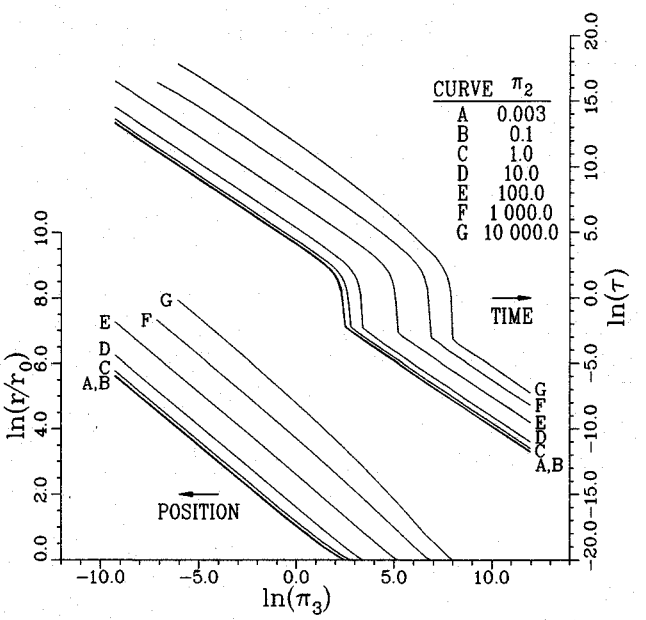

Fig. 5b Particle time and position at 3% velocity bias ($\pi_1 = 1.0$).

model geometry at slightly different flight conditions than the experimental case, two-dimensional cross sections of a portion of the delta wing flowfield calculated by Webster and Shang[11] are shown in Fig. 11. As represented by the 15 and 40% chord locations, the general form of the primary and secondary vortices appear to vary only slightly with chord, although the size of the structures varies proportionally with the wing span.

As an attempt to seed the inner core of the vortex, seed particles were initially positioned in the vicinity of the leading edge of the model. It was found, however, that the vertical momentum of the particles from the freestream angle of attack is too great. The particles enter the lower portion of the forming vortex, and continue to move vertically upward through the core and into the outer portion of the vortex before the initial vertical momentum is dissipated. By trial-and-error, it was found that the seed which penetrates deepest into the vortex core are particles that are swept around the edge of the wing from the underside.

Trajectories of seed particles that are initially positioned along the edge of the wing at 15% chord are shown in Fig. 12. As

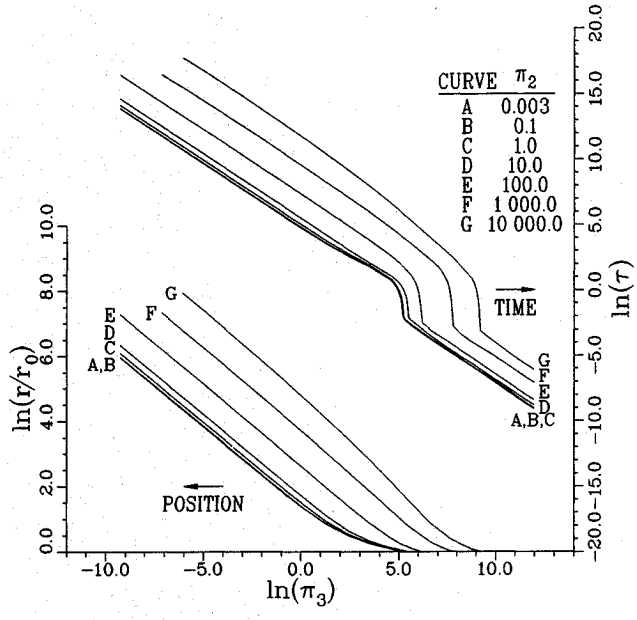

Fig. 5c Particle time and position at 3% velocity bias (π_1 = 2.0).

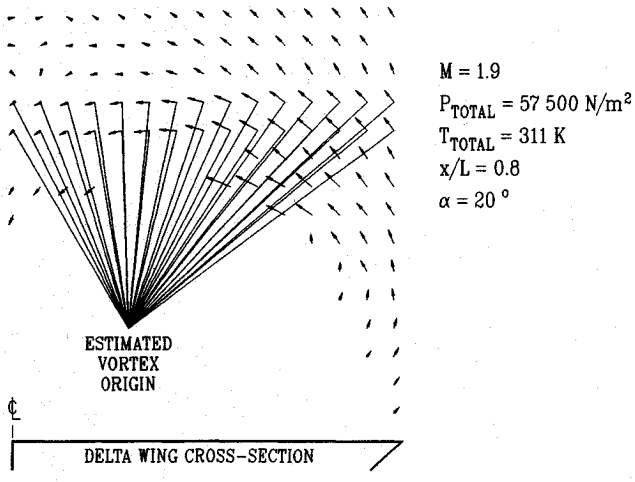

Fig. 6 LV measured velocity field produced by a delta wing (Ref. 5).

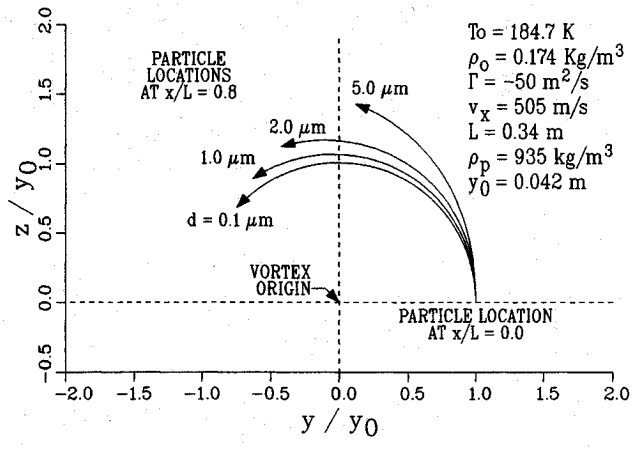

Fig. 7 Two-dimensional projection of silicon oil seed particle trajectories within a modeled delta wing vortex.

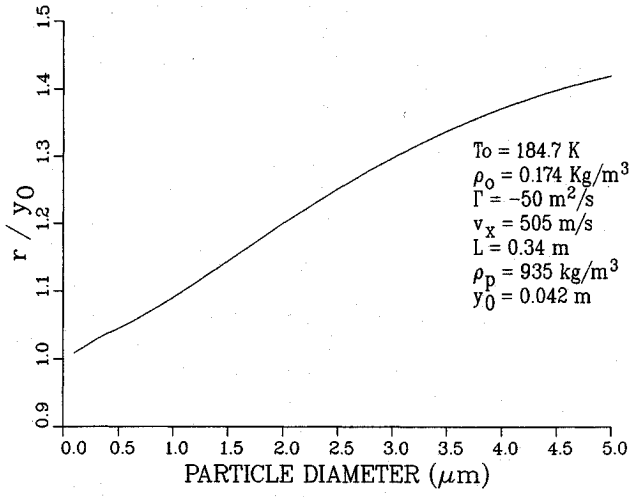

Fig. 8 Radial particle position at 80% chord within a modeled delta wing vortex.

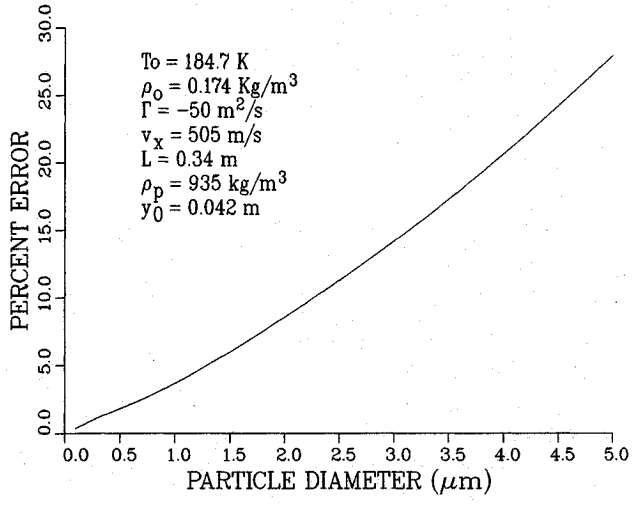

Fig. 9 Magnitude of velocity bias at 80% chord within a modeled delta wing vortex.

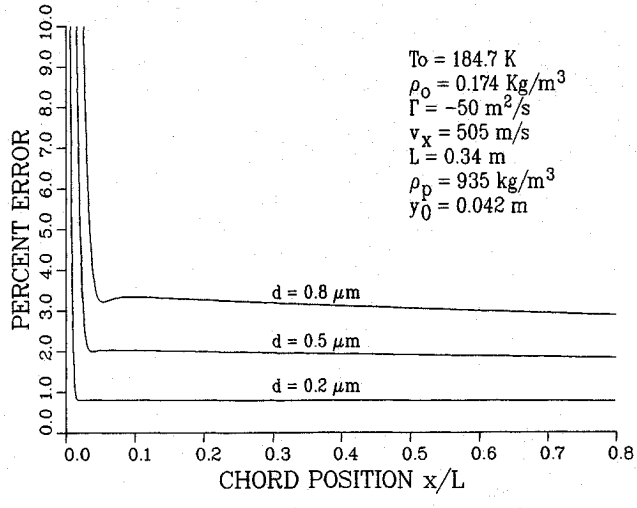

Fig. 10 Magnitude of velocity bias as a function of chord position within a modeled delta wing vortex.

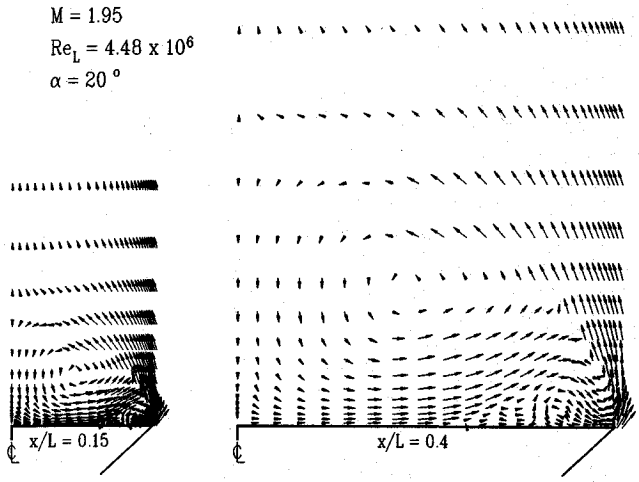

Fig. 11 Cross sections of a computationally derived vortical flowfield produced by a delta wing (Ref. 11).

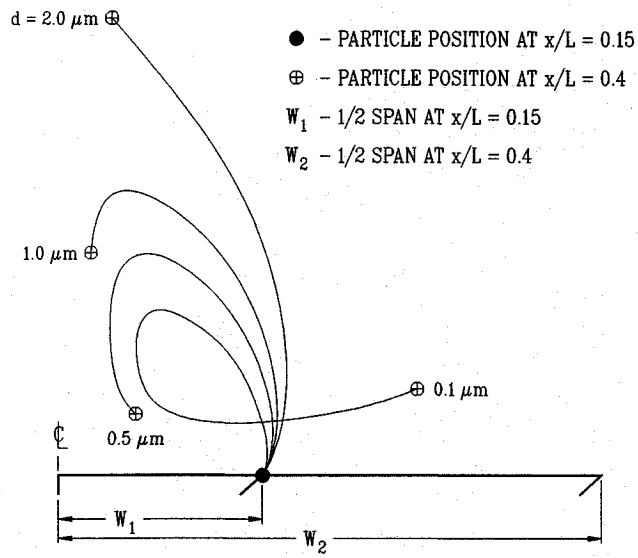

Fig. 12 Two-dimensional projection of silicon oil seed particle trajectories within a computationally derived delta wing flowfield.

the particles travel downstream, they are swept around the primary vortex. The smallest particle shown, 0.1 μm, completes an entire helical revolution prior to reaching the 40% chord station, and maintains a velocity bias of less than 3%. The 2.0-μm particle, on the other hand, is centrifuged out of the vortex, and has a final velocity bias of over 50%.

Trajectories for 0.2-μm particles at different initial chord locations along the edge of the wing are shown in Fig. 13. In each case, the particles are traveling helically around the primary vortex, which is growing chordwise. The particle that starts at the 5% chord location is shown to travel once around the primary vortex, and then it breaks off to circle the secondary vortex. As that particle moves beyond the 40% chord location shown, it passes back from the secondary to the primary vortex.

If the 40% chord positions of each of the particles shown in Fig. 13 are connected, the resulting curve will be the inner core bound for the seed found at that profile location. This curve is shown in Fig. 14 for three particle diameters. As would be expected, the size of the unseeded inner core grows with the size of the seed. The 0.5-μm particles travel slightly less than one helical revolution, and have an average velocity bias at 40% chord of about 10%. The 0.2-μm particles have an average velocity bias of around 5%, and the seed that starts near the leading edge is shown to be circling the secondary

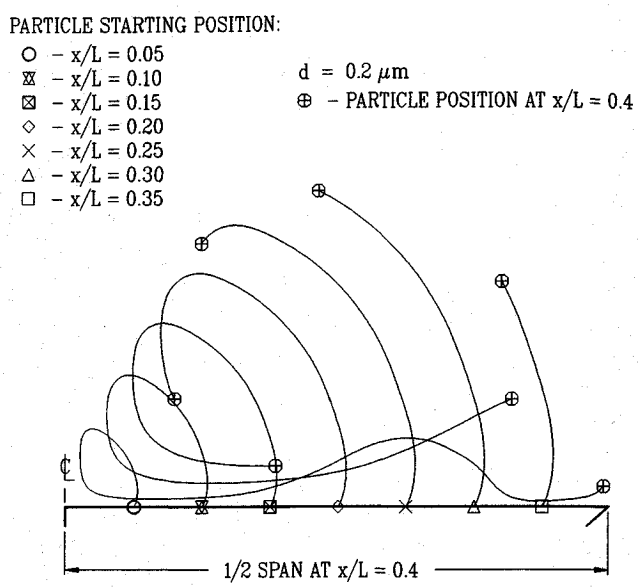

Fig. 13 Three-dimensional projection of silicon oil seed particle trajectories within a computationally derived delta wing flowfield. Each particle is initially at the outer edge of the wing.

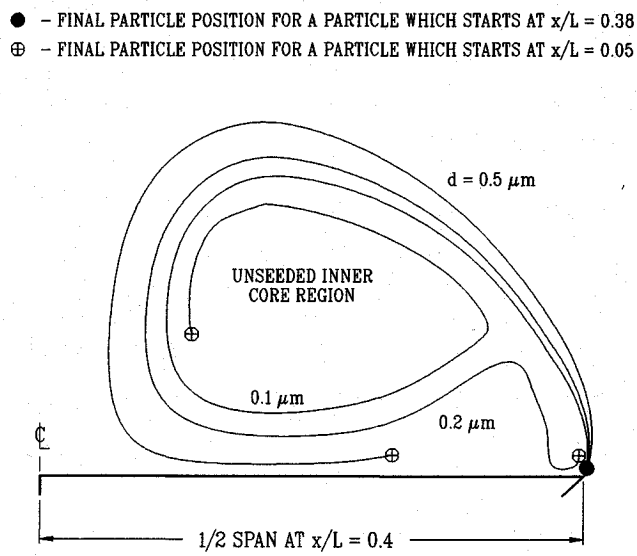

Fig. 14 Inner bounds of a silicon oil seeded flowfield at 40% chord within a computationally derived delta wing vortex.

vortex at the 40% chord location. The 0.1-μm seed, with an average velocity bias of about 3%, is entirely within the primary vortex at the 40% chord measurement station. Although the specific submicron particle size distribution of the experimental study is not known, the size and shape of the unseeded core, as determined by the LV surveys and laser light sheet visualization, correspond qualitatively with the analytical prediction.

Conclusions

Three contributions were made by this study. First, a three-dimensional potential vortex flowfield was developed and bounded for use as a mathematical model. Second, curves were presented that can be used to aid in the design and analysis of LV measurements in vortical flows over a large practical range of interest. Third, the particle equations of motion were coupled with a CFD-derived flowfield, showing the capability to numerically track the position and velocity bias of LV seed through highly complex flows.

Although the potential vortex is a very simple model of the delta wing vortex structure, it gave valuable insight into the behavior of the silicon oil seed in the wind-tunnel environment. It estimated the required particle diameter to within the same order of magnitude as using the CFD solution, and offers results for the entire class of solutions in terms of three dimensionless variables.

Tracking the particles through the CFD-generated flowfield offers the greatest potential to investigate seed density distributions and particle bias in any LV study which is coupled with a CFD effort. Using the RKF method of numerical integration to automatically adjust the time step based on equation stiffness makes the method numerically stable and efficient.

Both methods predict that the velocity bias within the delta wing vortex increases rapidly with particle diameter. Consequently, particle size must be carefully controlled in order to minimize particle dynamic bias. Future efforts will use the potential vortex model to design experiments and analyze data for vortical flows that do not have a companion CFD solution. When a CFD solution exists, it will be used with the particle equation of motion as a more precise method of quantifying the dynamic measurement bias.

Acknowledgments

The author thanks Dean Miller, George Seibert, Linda Smith, and Charles Tyler, who each contributed towards the collection and presentation of the LV measured flowfield, and also to Phillip Webster, who provided a complete numerical flowfield solution for this analysis.

References

[1]Nichols, R. H., "Calculation of Particle Dynamics Effects on Laser Velocimetry Data," *Wind Tunnel Seeding Systems for Laser Velocimeters*, NASA CP2393, March 1985, pp. 1–11.

[2]Hjelmfelt, A. T., Jr., and Mockros, L. F., "Motion of Discrete Particles in a Turbulent Fluid," *Applied Scientific Research*, Vol. 16, 1966, pp. 149–161.

[3]Schwind, R. G., and Mullen, J., Jr., "Laser Velocimeter Measurements of Slender-Body Vortices," AIAA Paper 79-0302, New Orleans, LA, Jan. 1979.

[4]Abid, R., and Schmitt, R., "Experimental Study of a Turbulent Horseshoe Vortex Using a Three Component Laser Velocimeter," AIAA Paper 86-1069, Atlanta, GA, May 1986.

[5]Smith, L. G., Maurice, M. S., Seibert, G. L., and Tyler, C., "Laser Velocimetry Measurements of Supersonic Vortex Flows on a Simple Razor-Edged Delta Wing," AIAA Paper 91-1684, Honolulu, HI, June 1991.

[6]Dring, R. P., and Suo, M., "Particle Trajectories in Swirling Flows," *Journal of Energy*, Vol. 2, No. 4, 1978, pp. 233–237.

[7]Chow, C.-Y., and Kuethe, A. M., *Foundations of Aerodynamics: Basis of Aerodynamic Design*, 3rd ed., Wiley, New York, 1976, pp. 20–58, 422–426.

[8]Anderson, J. D., Jr., *Fundamentals of Aerodynamics*, McGraw-Hill, New York, 1984, pp. 21–26, 152–155.

[9]Nichols, R. H., "The Effect of Particle Dynamics on Turbulence Measurements with a Laser Doppler Velocimeter," Ph.D. Dissertation, Dept. of Aerospace Engineering, Univ. of Tennessee, Knoxville, TN, June 1986.

[10]Crowe, C. T., "Drag Coefficient of Particles in a Rocket Nozzle," *AIAA Journal*, Vol. 5, No. 5, 1967, pp. 1021–1022.

[11]Webster, W. P., and Shang, J. S., "Comparison Between Thin Layer and Full Navier-Stokes Simulations Over a Supersonic Delta Wing," AIAA Paper 90-0589, Reno, NV, Jan. 1990.